UC Berkeley
UC Berkeley Previously Published Works

Title
Additive effects of acidification and mineralogy on calcium isotopes in Triassic/Jurassic boundary limestones

Permalink
https://escholarship.org/uc/item/4916s0cf

Journal
Geochemistry Geophysics Geosystems, 18(1)

ISSN
1525-2027

Authors
Jost, Adam B
Bachan, Aviv
van de Schootbrugge, Bas
et al.

Publication Date
2017

DOI
10.1002/2016gc006724

Peer reviewed

1　　**Additive effects of acidification and mineralogy on calcium isotopes in**
2　　**Triassic/Jurassic boundary limestones**

3　**Adam B. Jost[1]*, Aviv Bachan[1], Bas van de Schootbrugge[2], Shaun T. Brown[3,4], Donald J.**
4　**DePaolo[3,4], and Jonathan L. Payne[1]**

5　[1]Department of Geological Sciences, Stanford University, 450 Serra Mall, Bldg. 320, Stanford,
6　CA 94305 USA. [2]Department of Earth Sciences, Utrecht University, Marine Palynology &
7　Paleoceanography Group, Heidelberglaan 2, 3584 CS Utrecht, Netherlands. [3]Department of
8　Earth and Planetary Sciences, University of California, Berkeley, 307 McCone Hall, Berkeley,
9　CA 94720 USA. [4]Geochemistry Department, Earth Science Division, Lawrence Berkeley
10　National Laboratory, 1 Cyclotron Rd., Berkeley, CA 94720 USA.

11　Corresponding author: Adam B. Jost (abjost@mit.edu)

12　*Current address: Department of Earth, Atmospheric, and Planetary Sciences, Massachusetts
13　Institute of Technology, 77 Massachusetts Ave. 54, Cambridge, MA 02139 USA.

14　**Key Points:**

15　• We observe a large negative calcium isotope excursion above the Triassic/Jurassic
16　boundary.

17　• Numerical modeling indicates the excursion is too large to be attributed to ocean
18　acidification alone.

19　• Much of the excursion is due to higher proportions of aragonite in our samples, possibly
20　favored during recovery from acidification.
21

22   **Abstract**

23   The end-Triassic mass extinction coincided with a negative $\delta^{13}C$ excursion, consistent with

24   release of ^{13}C-depleted CO_2 from the Central Atlantic Magmatic Province. However, the amount

25   of carbon released and its effects on ocean chemistry are poorly constrained. The coupled nature

26   of the carbon and calcium cycles allows calcium isotopes to be used for constraining carbon

27   cycle dynamics and vice versa. We present a high-resolution calcium isotope ($\delta^{44/40}Ca$) record

28   from 100 m of marine limestone spanning the Triassic/Jurassic boundary in two stratigraphic

29   sections from northern Italy. Immediately above the extinction horizon and the associated

30   negative excursion in $\delta^{13}C$, $\delta^{44/40}Ca$ decreases by ca. 0.8‰ in 20 m of section and then recovers

31   to pre-excursion values. Coupled numerical models of the geological carbon and calcium cycles

32   demonstrate that this $\delta^{44/40}Ca$ excursion is too large to be explained by changes to seawater

33    $\delta^{44/40}Ca$ alone, regardless of CO_2 injection volume and duration. Less than 20% of the $\delta^{44/40}Ca$

34   excursion can be attributed to acidification. The remaining 80% likely reflects a higher

35   proportion of aragonite in the original sediment, based largely on high concentrations of Sr in the

36   samples. Our study demonstrates that coupled models of the carbon and calcium cycles have the

37   potential to help distinguish contributions of primary seawater isotopic changes from local or

38   diagenetic effects on the $\delta^{44/40}Ca$ of carbonate sediments. Differentiating between these effects is

39   critical for constraining the impact of ocean acidification during the end-Triassic mass

40   extinction, as well as for interpreting other environmental events in the geologic past.

41   **1 Introduction**

42   The end-Triassic mass extinction (ca. 201.6 Ma) was one of the five most severe biotic

43   crises of the Phanerozoic [*Raup and Sepkoski*, 1982]. Ocean acidification has been invoked as a

44   kill mechanism based on the preferential loss of heavily calcified marine animals [*Hautmann*,

45   2006; *Kiessling and Simpson*, 2011; *McRoberts et al.*, 2012] and a decrease in $CaCO_3$ deposition

46   in marine stratigraphic sections [*Hautmann*, 2004]. The extinction is coeval with the

47   emplacement of the Central Atlantic Magmatic Province (CAMP) [*Blackburn et al.*, 2013], an

48   increase in atmospheric pCO_2 [*Schaller et al.*, 2011; *Steinthorsdottir et al.*, 2011], and a negative

49   excursion in the $\delta^{13}C$ of $CaCO_3$ and organic matter [see *Bartolini et al.*, 2012; *Greene et al.*,

50   2012] suggesting the release of CO_2 from CAMP triggered the loss of marine life. However, the

51   amount of carbon released and the extent of resulting ocean acidification remains poorly

52   quantified. Determining the mass and isotopic composition of carbon release during the end-

53   Triassic mass extinction is critical both to pinpointing the source of carbon and to quantifying the

54   degree of ocean acidification.

55   Some studies have attempted to constrain release volumes using pCO_2 proxies [*Beerling

56   and Berner*, 2002], but these data have low temporal resolution and may not capture the highest

57   concentrations of pCO_2 that occurred during and immediately after injection. Two recent studies

58   have attempted to accurately replicate the $\delta^{13}C$ record by modeling pulsed releases of CO_2 from

59   CAMP[*Bachan and Payne*, 2015; *Paris et al.*, 2016], but neither study includes model

60   verification using a second geochemical record. Testing extinction scenarios that are constructed

61   to explain carbon isotope data against their predictions for additional isotopes systems is one

62   effective avenue towards better understanding the sequence of events during the Triassic-Jurassic

63   transition.

64   The calcium cycle is linked to the carbon cycle through burial of $CaCO_3$ and dependency

65   between weathering of Ca-bearing minerals and atmospheric pCO_2. Paired $\delta^{13}C$ and $\delta^{44/40}Ca$

66 records can potentially be used to quantify the amount and composition of carbon required for a
67 negative $\delta^{13}C$ excursion and to test the hypothesis of ocean acidification [*Payne et al.*, 2010a;
68 *Komar and Zeebe*, 2011, 2016; *Griffith et al.*, 2015]. Under acidification, excess volcanic CO_2
69 dissolves into seawater, shifting the distribution of dissolved carbonate species away from CO_3^{2-}
70 and decreasing the saturation state of $CaCO_3$ (Ω). $CaCO_3$ precipitation fractionates calcium
71 isotopes and favors ^{40}Ca over ^{44}Ca. As a result, a relative decrease in $CaCO_3$ burial results in less
72 preferential removal of ^{40}Ca from seawater and would cause a negative excursion in $\delta^{44/40}Ca$
73 beginning at the time of carbon release [*Payne et al.*, 2010b]. In addition, increased weathering
74 and seafloor dissolution of $CaCO_3$ as a consequence of high pCO_2 and reduced Ω, respectively,
75 would add isotopically light calcium to seawater. Similarly, $\delta^{13}C$ can be used to place broader
76 constraints on mechanisms underlying $\delta^{44/40}Ca$ variation. Paired data that cannot be explained by
77 any plausible environmental scenario can be used to identify cases in which one or both isotope
78 records are unlikely to represent ancient seawater or atmospheric compositions, but instead
79 reflect degree of influence from local or diagenetic effects.

80 With the goal of better constraining the nature of carbon release and the severity of ocean
81 acidification, we present new $\delta^{44/40}Ca$ data paired with previously published $\delta^{13}C$ data [*Bachan et*
82 *al.*, 2012, 2014] from samples collected at two sections spanning the end-Triassic extinction and
83 Early Jurassic recovery from the Lombardy Basin in Italy. We then use numerical simulations of
84 CO_2 injection into a coupled model of the carbon and calcium cycles to constrain the
85 mechanisms responsible for $\delta^{13}C$ and $\delta^{44/40}Ca$ variations.
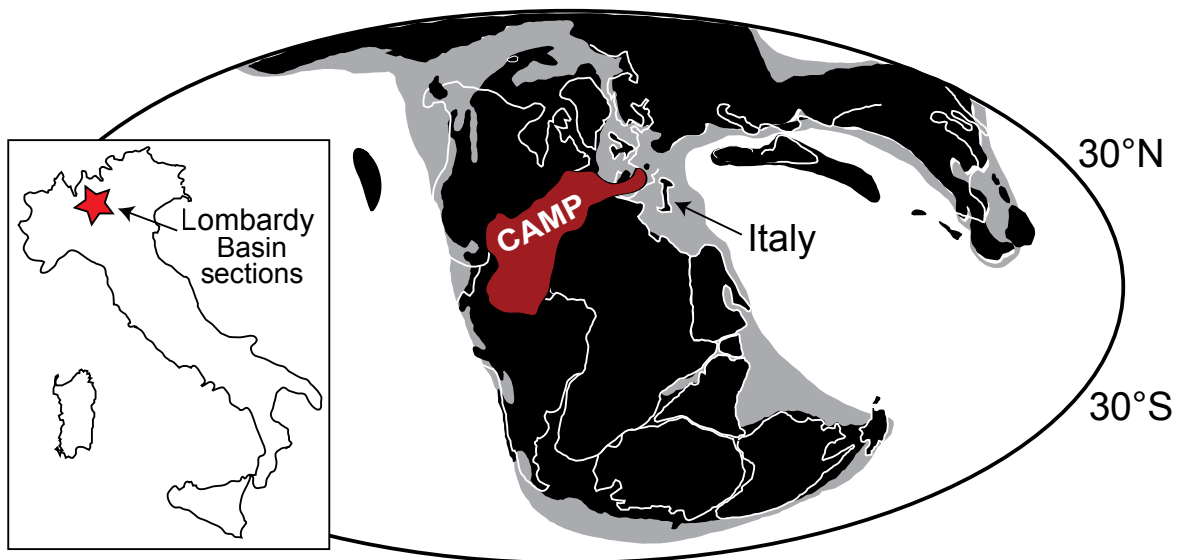
86

87 **Figure 1.** Paleogeographic reconstruction ca. 200 Ma showing the extent of CAMP and the location of Italy. Inset
88 shows the location of the Lombardy Basin in Italy, where the Val Adrara (45°43'29.33"N, 9°57'32.29"E) and

89   Italcementi (45°46'35.48"N, 9°30'27.09"E) sections are located. Modified from *van de Schootbrugge et al.* [2008]
90   and *Bachan et al.* [2012].

2 Materials and Methods

92   2.1 Geologic Setting

93   The Val Adrara and Italcementi sections are located in the Lombardy Basin of northern
94   Italy (Fig. 1). The two sections are separated by 35 km, with Val Adrara representing a more
95   distal setting on a shallowly dipping, subtidal ramp. Each section spans approximately 100 m of
96   stratigraphy, including the T/J boundary [*Bachan et al.*, 2012]. Facies successions are similar
97   between the two sections. Both sections have previously been studied for sedimentology,
98   paleontology and δ^{13}C stratigraphy [see *Bachan et al.*, 2012].

99   Both sections begin in the uppermost Triassic (Rhaetian) Zu limestone, which is
100   composed of algal, molluscan, and coralline packstone and wackestone. Rhaetian fossils,
101   including the Rhaetian pollen taxon *Rhaetipollis germanicus*, last occur in the uppermost Zu
102   limestone and are absent from the overlying Malanotte Formation (Fm.) [*Galli et al.*, 2005]. At
103   these sections, the Malanotte Fm. is interpreted as lowermost Hettangian in age based on the
104   acme of *Krauselisporites reissingeri* and the accompanying assemblage of other Hettangian-age
105   pollen taxa [*Galli et al.*, 2007]. The base of the Malanotte Fm. contains a marl interval, followed
106   by thinly bedded limestones and alternating shales transitioning upwards to shallower facies with
107   more abundant bedforms and carbonate grains by the top of the formation [*Bachan et al.*, 2012].
108   The overlying Albenza Fm. comprises peloidal and oolitic packstone and grainstone with some
109   molluscan material [*Bachan et al.*, 2012]. Correlation between the two sections is anchored by
110   the base of the lowermost Jurassic Malanotte Fm. We refined these correlations based on the
111   biostratigraphy of Galli et al. [2007] and the δ^{13}C data of *Bachan et al.* [2012].

112   2.2 Geochemical methods

113   We cut limestone samples using a tile saw and drilled micrite from cut faces for $\delta^{44/40}$Ca
114   and major/trace element analyses using a bench-top drill press equipped with a 0.8 mm dental
115   drill. Carbonate powders were digested overnight in 1 M acetic acid, centrifuged, and separated
116   from the insoluble fraction to avoid contamination from non-carbonate phases such as clays and
117   organic matter. After separation from the insoluble fraction, carbonate samples were dried and
118   redissolved in 3.0 M HNO_3. Dissolved samples were then spiked with a ^{42}Ca- and ^{48}Ca-enriched
119   tracer to allow for correction of mass-dependent fractionation occurring during analysis. Typical
120   ^{42}Ca/^{44}Ca ratios of spiked samples were 2–3. Calcium was purified from the sample matrix using
121   DGA resin (Eichrom). Samples were loaded on the resin in 3 M HNO_3 and the matrix was eluted
122   with subsequent additions of 3 M HNO_3 to the column. Calcium was then eluted using DI H_2O,
123   dried down and treated with concentrated HNO_3 to destroy residual organics from the resin. For
124   each analysis, approximately 3 μg of the purified calcium sample was loaded onto zone-refined
125   Re in a double filament configuration. Samples were run in a Thermo-Fisher Triton multi-
126   collector thermal ionization mass spectrometer (TIMS) at the Center for Isotope Geochemistry
127   (CIG), University of California, Berkeley. $\delta^{44/40}$Ca values are reported relative to Bulk Silicate
128   Earth (BSE) (^{40}Ca/^{44}Ca = 47.162 and ^{42}Ca/^{44}Ca = 0.31221) in standard δ-notation. NIST SRM-

129 915a is $-1.00‰$ on the BSE scale and seawater is $+0.91‰$ [*Nielsen et al.*, 2011]. SRM-915A
130 averaged $-1.03‰$ during this study and the long term reproducibility at CIG is ~0.1‰.

131   Concentrations of major and trace elements (Ca, Mg, Mn, Sr) were measured with an
132 inductively coupled plasma optical emission spectrometer (ICP-OES) in the Environmental
133 Measurements Lab at Stanford University. Carbon isotopes from both sections were measured
134 and presented by *van de Schootbrugge et al.* [2008] and *Bachan et al.* [2012, 2014]. *Bachan et*
135 *al.* [2012] labeled the initial negative excursion (N1), and two subsequent positive excursions
136 (P1 and P2) in the southern Alps. The N1 and P1 excursions are present within both sections in
137 this study (Fig. 2), and the P2 excursion is present at Val Adrara, albeit above our study interval.

3 Results

139   The two measured sections exhibit similar records of stratigraphic variation in $\delta^{44/40}Ca$
140 (Table 1, Fig. 2). At Val Adrara, $\delta^{44/40}Ca$ increases from $-0.77‰$ at the base of the section to $-$
141 $0.45‰$ at the Triassic/Jurassic (T/J) boundary. Just above the boundary, $\delta^{44/40}Ca$ decreases as low
142 as $-1.17‰$ in the Malanotte Fm. $\delta^{44/40}Ca$ then recovers to $-0.39‰$ in the uppermost Malanotte
143 above a stratigraphic gap, and ends at $-0.67‰$ in the lower Albenza Fm. At Italcementi, $\delta^{44/40}Ca$
144 starts at $-0.89‰$ at the base of the section, increases to $-0.26‰$ before the T/J boundary, and
145 then rapidly decreases to values as low as $-1.13‰$ in the lower Malanotte Fm. The record at
146 Italcementi provides more detail in the upper Malanotte Fm., showing a steady recovery from the
147 nadir up to $-0.46‰$ by the base of the Albenza Fm. The section ends in the lower Albenza at $-$
148 $0.68‰$. In both sections, the onset of the negative $\delta^{44/40}Ca$ excursion coincides with the N1
149 excursion in the $\delta^{13}C$ record. The nadir of the $\delta^{44/40}Ca$ excursion occurs approximately 5 m above
150 the peak of the P1 excursion in $\delta^{13}C$.
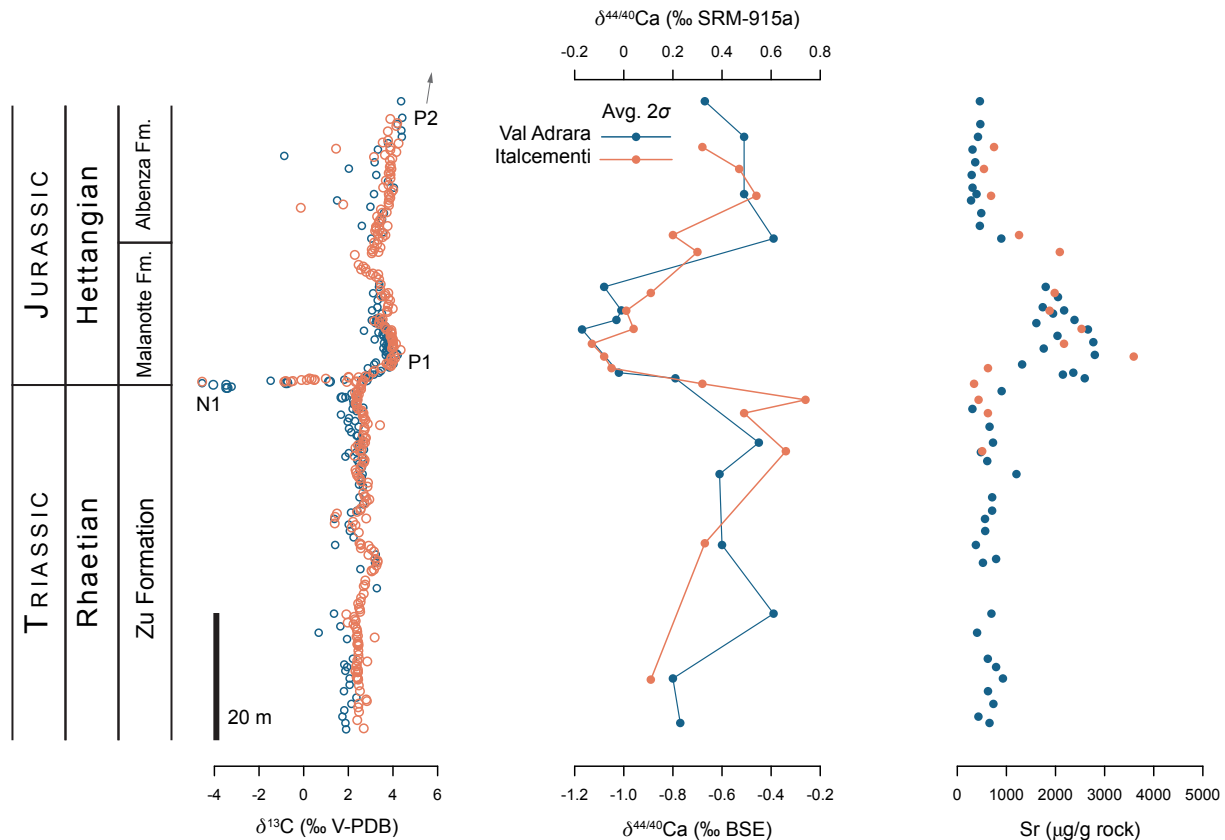
Figure 2. The $\delta^{13}C$, $\delta^{44/40}Ca$, and [Sr] data from each section, exhibiting large excursions immediately above the Triassic/Jurassic boundary. Dark blue is Val Adrara, orange is Italcementi. Val Adrara data are plotted by stratigraphic height, and Italcementi points are minimally adjusted to best match the $\delta^{13}C$ at Val Adrara. Errors on $\delta^{44/40}Ca$ are calculated from replicate measurements of the same sample.

Stratigraphic variations in [Sr] are also similar between the two sections (Table 1, Fig. 2). Both exhibit uppermost Triassic baseline [Sr] values near 650 ppm (μg/g rock), followed by a sharp rise to ca. 2800 ppm and a steady decrease back to baseline concentrations in the lower Albenza Fm. The [Sr] and $\delta^{44/40}Ca$ values are inversely correlated at both locations (Val Adrara: Spearman's $\rho = -0.71$, $p = 0.002$; Italcementi: $\rho = -0.76$, $p = 0.001$) (see Table S1 for all correlation coefficients).

4 Discussion

The co-occurrence of the negative $\delta^{44/40}Ca$ excursion with a rapid negative excursion in $\delta^{13}C$ and the last occurrences of Triassic fossils and the carbonate-poor boundary marl is consistent with an acidification scenario for the mass extinction event. To explore the extent to which acidification can account quantitatively for the coupled variations in $\delta^{44/40}Ca$ and $\delta^{13}C$, we simulated CO_2 injection using a coupled numerical model of the geological carbon and calcium cycles. Our model, similar to one introduced by Bachan and Payne [2015], uses mass and isotopic fluxes of carbon and calcium in a single ocean-atmosphere reservoir.

Table 1. Geochemical data from Val Adrara and Italcementi. For full $\delta^{13}C$ data, see *Bachan et al.* [2012, 2014]. 2σ values for $\delta^{44/40}Ca$ are calculated from replicate measurements of the same sample. Standard deviations on Ca, Mg,

172 Sr, and Mn measurements based on standard replicate measurements are 0.6 wt%, 0.03 wt%, 1 µg/g rock, and 3 µg/g
173 rock, respectively.

Stratigraphic height (m)	$\delta^{13}C$ (‰ VPDB)	$\delta^{18}O$ (‰ VPDB)	Ca (wt %)	Mg (wt %)	Sr (µg/g rock)	Mn (µg/g rock)	$\delta^{44/40}Ca$ (‰ BSE)	$\delta^{44/40}Ca$ (‰ SRM-915a)	$\delta^{44/40}Ca$ (‰ seawater)	2σ for $\delta^{44/40}Ca$	n for $\delta^{44/40}Ca$
Val Adrara											
2.8	1.87	-2.14	31.60	0.66	656	77	-0.77	-1.77	0.14	0.25	3
9.8	2.06	-2.19	31.00	0.57	929	73	-0.80	-1.80	0.11	0.11	2
20.0	1.36	-2.26	31.30	0.67	695	152	-0.39	-1.39	0.52	0.24	2
30.8	1.41	-3.52	29.70	0.66	378	68	-0.60	-1.60	0.31	0.17	2
40.0	2.64	-1.90	32.10	0.47	1204	26	-0.61	-1.61	0.30	0.03	2
46.9	2.54	-2.02	31.40	0.55	727	26	-0.45	-1.45	0.46	0.33	4
57.0	2.76	-2.56	33.67	0.40	2595	126	-0.79	-1.79	0.12	0.21	3
57.9	3.37	-1.68	34.74	0.41	2362	42	-1.02	-2.02	-0.11	0.13	2
64.7	3.79	-2.11	32.30	0.43	2660	74	-1.17	-2.17	-0.26	0.08	2
66.2	3.27	-3.20	35.39	0.32	2386	70	-1.03	-2.03	-0.12	0.16	2
67.7	3.06	-2.94	32.87	0.31	2175	87	-1.01	-2.01	-0.10	0.26	5
71.4	3.37	-2.59	33.20	0.41	1800	54	-1.08	-2.08	-0.17	0.08	2
79.0	3.03	-3.40	35.00	0.56	896	29	-0.39	-1.39	0.52	0.25	3
86.0	3.15	-5.84	35.35	0.66	392	13	-0.51	-1.51	0.40	0.13	2
95.0	4.40	-5.32	34.40	0.16	421	7	-0.51	-1.51	0.40	0.08	2
100.6	4.36	-5.68	33.50	1.29	460	13	-0.67	-1.67	0.24	0.17	2
Italcementi											
7.4	2.44	-1.40	NA	NA	NA	NA	-0.89	-1.89	0.02	0.14	2
23.9	2.50	-1.54	NA	NA	NA	NA	-0.67	-1.67	0.24	0.23	3
35.4	2.51	-1.59	20.30	0.50	507	513	-0.34	-1.34	0.57	0.47	3
41.1	2.68	-4.48	31.03	0.43	623	21	-0.51	-1.51	0.40	0.01	2
43.1	2.42	-2.91	35.98	0.30	433	19	-0.26	-1.26	0.65	0.04	2
45.5	2.58	-1.99	35.79	0.48	341	21	-0.68	-1.68	0.23	0.16	2
47.1	3.49	-1.88	26.08	0.71	624	111	-1.05	-2.05	-0.14	0.11	2
49.9	NA	NA	44.43	0.59	3592	85	-1.08	-2.08	-0.17	0.06	2
53.0	NA	NA	31.09	0.33	2173	38	-1.13	-2.13	-0.22	0.34	2
56.6	3.68	-1.92	39.76	0.41	2531	59	-0.96	-1.96	-0.05	0.11	2
61.0	3.73	-2.19	39.76	0.36	1880	74	-0.99	-1.99	-0.08	0.24	2
65.3	3.79	-2.56	31.26	0.31	1983	47	-0.89	-1.89	0.02	0.23	3
72.9	3.35	-2.14	30.44	0.31	2087	50	-0.70	-1.70	0.21	0.07	2
77.0	3.66	-2.05	35.67	0.59	1257	25	-0.80	-1.80	0.11	0.35	2
86.5	3.83	-2.58	35.76	0.45	687	15	-0.46	-1.46	0.45	0.18	2
93.0	3.93	-3.97	36.52	0.37	543	13	-0.53	-1.53	0.38	0.00	2
98.3	3.88	-6.70	34.89	0.37	748	7	-0.68	-1.68	0.23	0.24	2

174

175 CAMP likely erupted in four pulses [*Schaller et al.*, 2011] over the early-middle
176 Hettangian (*spelae–liassicus* zones [*Hillebrandt et al.*, 2013]), or potentially into the late
177 Hettangian (*liassicus–angulata* zones [*Hillebrandt et al.*, 2013]) based on correlation of $\delta^{13}C$ in
178 northern Italy with geochronologically constrained sections elsewhere [*Bachan and Payne*,
179 2015]. The interval examined in this study encompasses the N1 and P1 excursions, which likely
180 corresponds to the first observed increase in pCO_2. If the N1 and P1 excursions were associated
181 with first rise in CO_2 observed by *Schaller et al.* [2011, 2012], then our study interval post T/J
182 boundary is likely constrained to 270 kyr. *Bachan and Payne* [2015] modeled this initial eruptive
183 phase using a two-pulse injection (4200 Pg C at −70‰ and 14,400 Gt C at −5.5‰). In this study,
184 we opt for a single pulse of CO_2 for simplicity.

185   4.1 Model construct

186   We constructed a forward box model of the carbon and calcium cycles to predict the
187 dynamics of these interconnected biogeochemical systems. The ocean is the sole reservoir in our
188 model, in which we track the moles of dissolved inorganic carbon (M_C), referred to in the text
189 hereafter as *DIC*, dissolved Ca^{2+} (M_{Ca}), dissolved phosphate (M_P), and dissolved sulfate (M_S).
190 The changes in M_C can be expressed in terms of the major inputs and outputs to the
191 ocean/atmosphere carbon reservoir:

192
$$\frac{dM_C}{dt} = F_{w,carb} + F_{w,org} + F_{volc} - F_{b,org} - F_{b,carb} \qquad \text{Eq. 1}$$

193 where $F_{w,carb}$ and $F_{b,carb}$ are the weathering and burial of calcium carbonate rock, $F_{w,org}$ and $F_{b,org}$
194 are the weathering and burial of organic carbon, and F_{volc} is the release of volcanic CO_2. We set
195 *DIC* and total alkalinity (*Alk*) to yield an initial pCO_2 value ~2000 ppm and a mean saturation
196 state of calcite, $\Omega_{calcite}$ (herein simply Ω) of 1.75 (see Table 2 for a list of parameters). The
197 changes in M_{Ca} can be expressed similarly:

198
$$\frac{dM_{Ca}}{dt} = F_{w,sil} + F_{w,carb} - F_{b,carb}$$
Eq. 2

199 where $F_{w,sil}$ is the weathering of Ca-bearing silicate rock. The initial concentration of Ca^{2+} is set
200 to 17 mM, yielding a residence time of approximately 650 kyr (determined as $M_{Ca}/F_{b,carb}$ during
201 steady state). Using equations from *Berner* [2004], we define the non-carbonate weathering
202 fluxes (Ca-silicates, and organic C) and carbonate fluxes such that they each scale with the
203 atmospheric pCO_2:

204
$$F_{w,t} = F_{w,i}(RCO_2)^{GZ}(1 + GZlog(RCO_2))^{0.65}$$
Eq. 3

205
$$F_{w,carb,t} = F_{w,carb,i}(RCO_2)^{GZ_{carb}}(1 + GZlog(RCO_2))$$
Eq. 4

206 where G and Z are constant scaling coefficients (see *Berner* [2004]) and RCO_2 is the ratio of CO_2
207 at time t relative to the level at the initial time i:

208
$$RCO_2 = \frac{pCO_{2,t}}{pCO_{2,i}}$$
Eq. 5

209 pCO_2 is calculated from the total dissolved inorganic carbon *(DIC)*, which is determined
210 from M_C:

211
$$DIC = \frac{M_C}{sV_{oc}}$$
Eq. 6

212 and alkalinity (*Alk*):

213
$$Alk = 2\frac{M_{Ca^{2+}}}{sV_{oc}} - 2\frac{M_{SO_4^{2-}}}{sV_{oc}} + k_{alk}$$
Eq. 7

214 where s is salinity, V_{oc} is ocean volume, and k_{alk} is a constant representing the remaining
215 components of alkalinity, which we assume to be fixed during the perturbation. Thus, with *Alk*
216 and *DIC* known, we solve for the other parameters of the carbonate system ($[CO_3^{2-}]$, $[HCO_3^-]$,
217 $[H_2CO_3]$, pCO_2, pH) based on the methods outlined in *Zeebe and Wolf-Gladrow* [2001]. The
218 burial flux of $CaCO_3$ scales with Ω:

219
$$\Omega = \frac{[Ca^{2+}][CO_3^{2-}]}{K_{sp}}$$
Eq. 8

220 where Ω values <1 imply undersaturation and dissolution, and $\Omega \geq 1$ implies saturation and
221 precipitation. Thus, the burial of carbonate scales with Ω:

222
$$F_{b,carb,t} = F_{b,carb,i}\frac{\Omega_t - 1}{\Omega_i - 1}$$
Eq. 9

223 Our model does not include a sediment reservoir, so we cannot explicitly dissolve $CaCO_3$
224 sediment during an acidification. However, if Ω drops below 1.0, $F_{b,carb}$ will become negative
225 and become an input into the ocean reservoir. This process simulates dissolution of $CaCO_3$ in the
226 absence of a dedicated sediment reservoir.

227 The burial of organic carbon is dependent on the relative changes in the amount of phosphate
228 (M_P), a limiting nutrient on geologic timescales, in seawater:

229 $$F_{b,org,t} = F_{b,org,i} k_{cp} \qquad \text{Eq. 10}$$

230 where k_{cp} is equivalent to the C:P ratio in ocean sediment:

231 $$k_{cp,t} = k_{cp,i} \left(\frac{M_{PO_4^{2-},t}}{M_{PO_4^{2-},i}} \right)^{p_{cp}} \qquad \text{Eq. 11}$$

232 and p_{cp} is a scaling coefficient (assumed to be unity for all scenarios in this study—see *Bachan*
233 *and Payne* [2015] for other uses). The C:P ratio in sediments is normally Redfieldian (106:1) in
234 oxic conditions, but low oxygen conditions favor release of PO_4^{3-} sorbed on Fe(III) oxides [*Van*
235 *Cappellen and Ingall*, 1996].

236 All of the carbon and calcium delivery and removal fluxes can be assigned an average
237 isotopic composition to be used in determining the change in seawater isotopic composition over
238 time:

239 $$M_C \frac{d\delta_C}{dt} = F_{volc}(\delta_{volc} - \delta_C) + F_{w,org}(\delta_{w,org} - \delta_C) + F_{w,carb}(\delta_{w.carb} - \delta_C) -$$
240 $$F_{b,org}(\Delta_{org}) \qquad \text{Eq. 12}$$

241 $$M_{Ca} \frac{d\delta_{Ca}}{dt} = (F_{w,sil} + F_{w,carb})(\delta_{w,riv} - \delta_{Ca}) - F_{b,carb}(\Delta_{carb}) \qquad \text{Eq. 13}$$

242 where δ_{riv} is the average riverine $\delta^{44/40}$Ca composition, calculated at each t based on the relative
243 contribution of $F_{w,carb}$ and $F_{w,sil}$. We incorporate a carbon injection via a new variable F_{extra} with
244 a δ^{13}C composition δ_{extra}. These are incorporated into Eqs. 1 and 11 such that:

245 $$\frac{dM_C}{dt} = F_{w,carb} + F_{w,org} + F_{volc} - F_{b,org} - F_{b,carb} + F_{extra} \qquad \text{Eq. 14}$$

246 $$M_C \frac{d\delta_C}{dt} = F_{volc}(\delta_{volc} - \delta_C) + F_{w,org}(\delta_{w,org} - \delta_C) + F_{w,carb}(\delta_{w.carb} -$$
247 $$\delta_C) - F_{b,org}(\Delta_{org}) + F_{extra}(\delta_{extra} - \delta_C) \qquad \text{Eq. 15}$$

248 Initial values and parameters for the model are listed in Table 2. Equations are based on
249 those in *Kump and Arthur* [1999], *Berner* [2004], *DePaolo* [2004], and *Bachan and Payne*
250 [2015]. Select output from a single model run is illustrated in Figure 3.

251
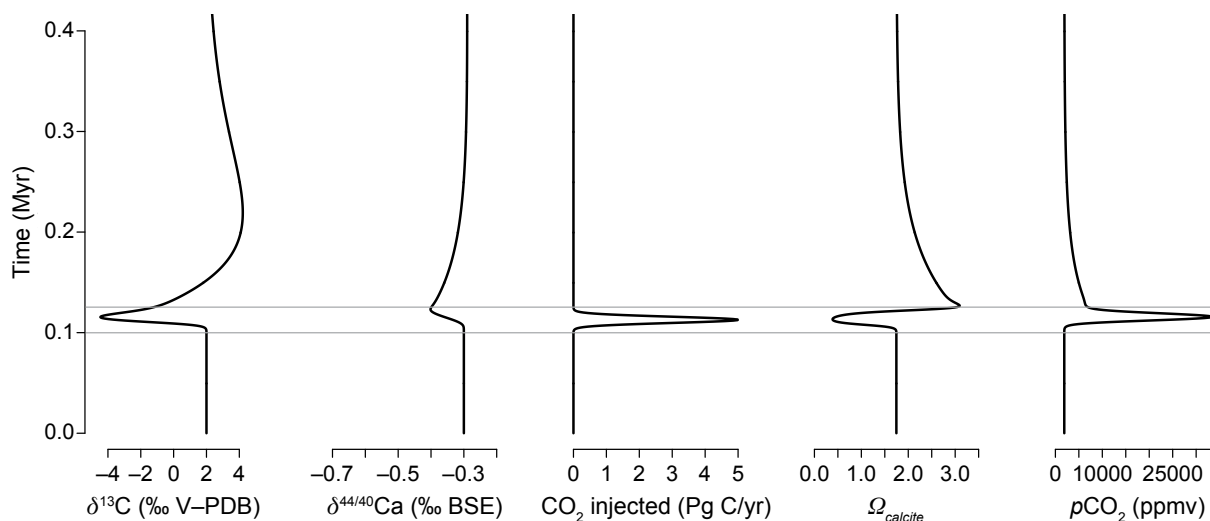
Figure 3. Output from a single model run illustrating the typical geochemical patterns resulting from a CO_2 perturbation in our model. From left to right, rate of CO_2 injection, $\delta^{13}C$, $\delta^{44/40}Ca$, $\Omega_{calcite}$, and pCO_2. This scenario depicts an injection of 40,000 Pg C with a $\delta^{13}C$ value of –15‰ injected over 25 kyr. The grey lines signify the start and end of the CO_2 injection.

256   4.2 Modeling results and the role of acidification in the excursion

257   We iteratively modeled a range of CO_2 injection volumes (from 5000 to 50,000 Pg C),
258   $\delta^{13}C$ compositions of injected CO_2 (from –5‰ (average mantle) to –60‰ (biogenic CH_4)), and
259   durations of CO_2 release (5 kyr to 50 kyr) assuming seawater [Ca] = 17 mM [*Horita et al.*, 2002]
260   (see supplement for consideration of alternative [Ca] values). We then compared the magnitudes
261   of the modeled negative and positive $\delta^{13}C$ excursions to the Val Adrara N1 and P1 $\delta^{13}C$
262   excursions (6.5 below and 2.3‰ above the first sampled $\delta^{13}C$ of 1.9‰) to determine the
263   optimum scenario. There are several parameter combinations that can recreate the N1 and P1
264   excursions; the optimum range is roughly 40,000 to 45,000 Pg C at –15‰ in less than 30 kyr
265   (Fig. 4). Importantly, these scenarios result in a negative $\delta^{44/40}Ca$ excursion only slightly larger
266   than 0.1‰. In fact, no model scenario within our entire model parameter space produces a
267   $\delta^{44/40}Ca$ excursion as large as is observed in our records (maximum modeled excursion is –
268   0.14‰) (Fig. 4). Note that we model organic carbon burial with a first order equation (p_{cp}=1),
269   whereas Bachan and Payne [2015] vary p_{cp} between 1 and 3 for different CO_2 pulses. Increasing
270   p_{cp} to 3 would increase the magnitude of the P1 excursion, thereby requiring less CO_2 to yield
271   the same size excursion. Because of this reduction in CO_2 required with increase p_{cp}, as well as
272   the fact that we are modeling this event as a single CO_2 pulse, our optimum CO_2 magnitudes
273   should be viewed as upper limits. According to our simulations, if the observed excursion in
274   $\delta^{44/40}Ca$ is –0.72‰ (based on Val Adrara; it is –0.87‰ at Italcementi), then at most 20% of the
275   observed negative excursion in $\delta^{44/40}Ca$ is attributable to CO_2 release and acidification, leaving
276   the remaining 80% to be explained by local or diagenetic mechanisms.

277

278   **Table 2.** Model parameters and initial variables.

Variable	Value	Units	Reference
T	15	°C	
s	1.035	kg/L	
V_{oc}	2.32×10^{21}	L	
Alk	1.89×10^{-3}	eq/kg	Used to generate correct $p\mathrm{CO_2}$ and Ω
DIC	1.90×10^{-3}	mol/kg	Used to generate correct $p\mathrm{CO_2}$ and Ω
initial [Ca]	17×10^{-3}	mol/kg	Based on Horita et al. 2002
initial [PO4]	25×10^{-6}	mol/kg	
initial [SO4]	28×10^{-3}	mol/kg	
initial Ω	1.75	—	
K_{sp}	4.31×10^{-7}	mol^2/kg^2	Calculated with Zeebe and Wolf-Gladrow (2001)
initial $p\mathrm{CO_2}$	1893	ppm	Based on Steinthorsdottir et al. 2011
initial k_{alk}	0.0243	—	Solved for based on Alk, [Ca], and [SO$_4^{3-}$]
initial $f_{w,org}$	0.25	—	
initial $f_{b,org}$	0.25	—	
F_{volc}	16×10^{12}	mol C/yr	Kump and Arthur 1999, adjusted for steady state
initial $F_{w,carb}$	24×10^{12}	mol CCa/yr	Kump and Arthur 1999, adjusted for steady state
initial $F_{w,org}$	8×10^{12}	mol C/yr	Kump and Arthur 1999, adjusted for steady state
initial $F_{w,sil}$	12×10^{12}	mol Ca/yr	Kump and Arthur 1999, adjusted for steady state
initial $F_{b,carb}$	36×10^{12}	mol CCa/yr	Kump and Arthur 1999, adjusted for steady state
initial C:P, k_{cp}	106	—	
initial $F_{b,org}$	12×10^{12}	mol C/yr	Kump and Arthur 1999, adjusted for steady state
initial $F_{w,p}$	11.3×10^{10}	mol P/yr	
initial $F_{b,p}$	11.3×10^{10}	mol P/yr	
G	3.3		Berner (2004)
Z	0.09		Berner (2004)
Z_{carb}	0.07		Berner (2004)
δ_{volc}	-5.5	‰ VPDB	Kump and Arthur 1999, adjusted for steady state
initial $\Delta_{C,org}$	30	‰	Kump and Arthur 1999, adjusted for steady state
initial $\delta_{b,carb}$	2	‰ VPDB	Based on data from this study
initial $\delta_{b,org}$	-28	‰ VPDB	Kump and Arthur 1999, adjusted for steady state
$\delta_{w,carb}$	2	‰ VPDB	Kump and Arthur 1999, adjusted for steady state
$\delta_{w,org}$	-28	‰ VPDB	Kump and Arthur 1999, adjusted for steady state
initial Δ_{Ca}	-1.4	‰	Calculated using Ω using Eqs. from DePaolo 2011
initial $\delta_{b,Ca}$	-0.3	‰ BSE	Based on data from this study
δ_{riv}	-0.3	‰ BSE	Calculated from relative contributions of F_{wcarb} and F_{wsil}
$\delta_{w,carb}$	-0.4	‰ BSE	Based on Depaolo 2004, adjusted for steady state
$\delta_{w,sil}$	-0.1	‰ BSE	Based on Depaolo 2004, adjusted for steady state

279

280

281   Many processes can influence a $\delta^{44/40}$Ca record, particularly variation in the magnitude of
282   calcium isotope fractionation ($\Delta^{44/40}$Ca) during CaCO$_3$ precipitation due to precipitation rate
283   [*Tang et al.*, 2008; *DePaolo*, 2011], stoichiometry [*Nielsen et al.*, 2012], mineralogy [*Gussone et*
284   *al.*, 2005; *Blättler et al.*, 2012], and temperature [*Gussone et al.*, 2005]. Diagenetic processes can
285   also alter the $\delta^{44/40}$Ca of carbonate sediments and rocks [*Holmden et al.*, 2012; *Fantle*, 2015].
286   The extent to which one or more of these processes can account for observed $\delta^{44/40}$Ca variation
287   can be assessed through comparison with predictions under these scenarios. In addition, many
288   scenarios imply predictions for the behavior of other aspects of rock chemistry, such as trace
289   element concentrations.

290   Submarine groundwater discharge (SGD) can be ruled out as a cause of the T/J boundary
291    $\delta^{44/40}$Ca excursion at our study site. SGD during marine regression can cause seawater to mix
292   with ^{44}Ca-depleted pore-fluids during precipitation and thereby lower its $\delta^{44/40}$Ca composition

293   [*Holmden et al.*, 2012]. However, the local sea level history is not compatible with this

294   explanation. The lowest $\delta^{44/40}$Ca values in our dataset occur in the Malanotte Fm., which

295   represents a transgression in the Lombardy Basin and much of western Europe [*Galli et al.*,

296   2007]. The subsequent return to higher $\delta^{44/40}$Ca values coincides with a transition into the lower

297   Albenza Fm. oolites and peloidal grainstones, which reflect local shallowing after the deposition

298   of the Malanotte Fm. Thus, changes in local base level are in the direction opposite to that

299   expected under an SGD scenario.

300   The magnitude of $\Delta^{44/40}$Ca is affected by temperature, precipitation rate (R), and

301   mineralogy. Temperature can be ruled out as the primary control because the observed $\delta^{44/40}$Ca

302   excursion would require a temperature decrease of approximately 35 °C (assuming 0.02‰/°C

303   [*Gussone et al.*, 2005]), which is unrealistically large and inconsistent with evidence for

304   increased pCO$_2$ and climate warming [*Schaller et al.*, 2011; *Steinthorsdottir et al.*, 2011].

305   Precipitation rate is not likely the driver of our $\delta^{44/40}$Ca record. In laboratory studies,

306   precipitation rates strongly affect the magnitude of $\Delta^{44/40}$Ca in inorganic calcite [*Lemarchand et*

307   *al.*, 2004; *Tang et al.*, 2008]. Assuming a constant seawater stoichiometry (Ca^{2+}:CO_3^{2-}), the

308   average $\Delta^{44/40}$Ca observed for CaCO$_3$ precipitated from modern seawater (ca. 1.4‰) is already

309   close to maximum observed kinetic value, and thus cannot increase in magnitude by more than

310   ca. 0.2‰ [*DePaolo*, 2011; *Nielsen et al.*, 2012]. Decreasing Ca^{2+}:CO_3^{2-} by orders of magnitude

311   could cause $\Delta^{44/40}$Ca to increase [*Nielsen et al.*, 2012], however our model only predicts a

312   decrease of ~40%. Furthermore, it is unclear exactly how this relationship applies to organisms

313   precipitating biogenic CaCO$_3$, as it would require them to vary their forward/backward/net

314   precipitation rates significantly in order to vary $\Delta^{44/40}$Ca noticeably. It remains unclear whether

315   precipitation rate and/or seawater stoichiometry affected carbonate sediment $\delta^{44/40}$Ca

316   significantly, but given the required assumptions, we view this scenario as unlikely.

317

318
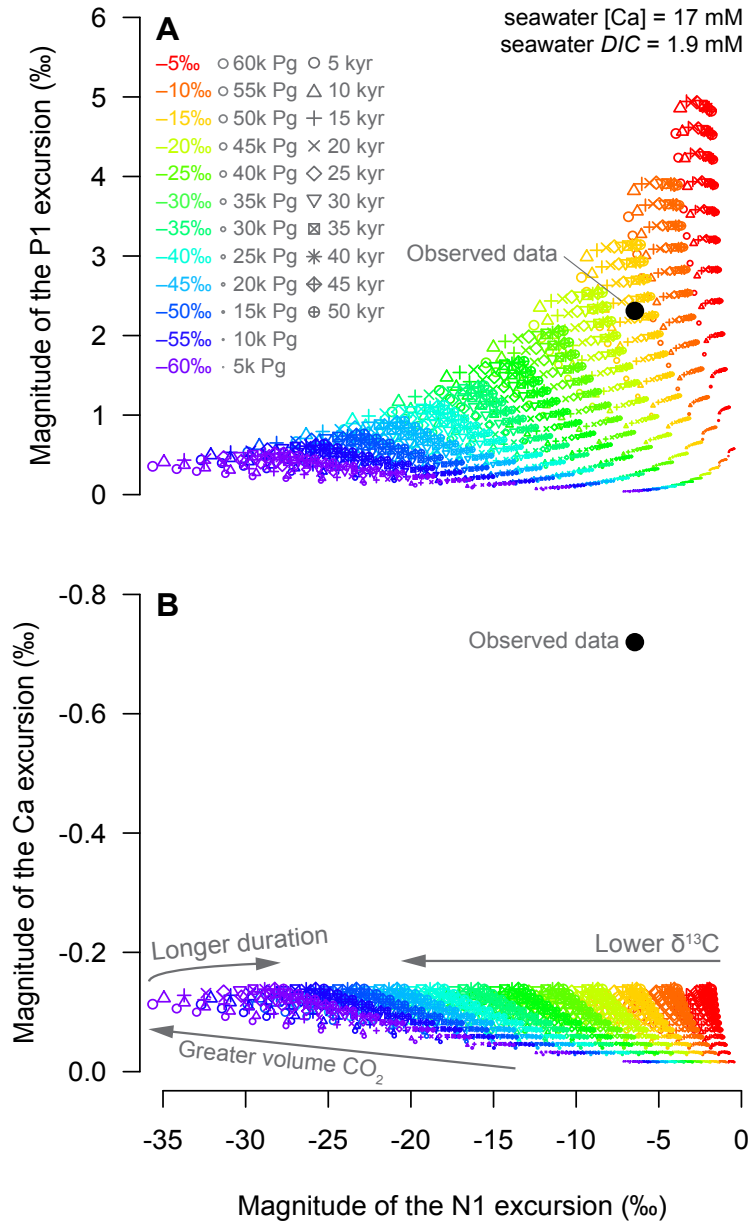
Figure 4. Model predicted (color) and observed (black) values for (A) the N1 and P1 $\delta^{13}C$ excursions and (B) the N1 $\delta^{13}C$ and $\delta^{44/40}Ca$ excursion, demonstrating that while the $\delta^{13}C$ data can be reconciled with modeled scenarios, the $\delta^{44/40}Ca$ data cannot. For the model outputs, symbol size corresponds to the volume of injected CO_2, symbol type corresponds to injection duration, and symbol color corresponds to the $\delta^{13}C$ of the injected CO_2. Model excursion magnitudes are relative to the pre-event baseline. Observed $\delta^{13}C$ excursion magnitudes are relative to the first sampled $\delta^{13}C$ value at Val Adrara. The observed $\delta^{44/40}Ca$ excursion magnitude is relative to the last data point (–0.45‰) before the excursion. While there is a range of scenarios that can replicate the $\delta^{13}C$ data, there are no models that can simultaneously replicate the $\delta^{44/40}Ca$ data.

A local increase in the proportion of aragonite (f_a) at our study locations could account for the direction and magnitude of the negative $\delta^{44/40}Ca$ excursion because the $\Delta^{44/40}Ca$ for

329 aragonite is as much as 0.9‰ greater than it is for calcite [*Gussone et al.*, 2005]. The higher [Sr]
330 in the Malanotte samples are also consistent with this scenario, as aragonite incorporates more Sr
331 than high- or low-Mg calcite does. However, this scenario alone does not account for the
332 contemporaneous changes in δ^{13}C. A global switch from calcite to aragonite seas is also a
333 possible cause for the excursion in $\delta^{44/40}$Ca [*Farkaš et al.*, 2007; *Blättler et al.*, 2012], but the
334 temporary increase in [Sr] is inconsistent with a permanent shift to aragonite. This scenario is
335 also at odds with existing sedimentological and paleontological evidence suggesting the Early
336 Jurassic oceans switched from aragonite to calcite seas [*Hautmann*, 2006; *Stanley*, 2006].

337 The observed changes in [Sr] are roughly compatible with variable f_a, as calcite has lower
338 concentrations (<1000 ppm) than aragonite does (ca. 7000 ppm) [*Veizer*, 1983]. Predicting how
339 these changes in [Sr] manifested is challenging because f_a (and [Sr]) can vary due to linear
340 mixing of primary aragonite and calcite or due to preferential diagenetic recrystallization of
341 aragonite to calcite (see supplement for an extended consideration of $\delta^{44/40}$Ca and [Sr]
342 covariation) [*Husson et al.*, 2015]. An upper limit on changing [Sr] can be determined from a
343 linear mixing; using the concentrations above, increasing f_a by 64% would yield a [Sr] increase
344 of 4000 ppm. This value is greater than the observed maximum [Sr], though some may have
345 been additionally lost during diagenesis [*Brand and Veizer*, 1980]. In either case, all of the
346 CaCO$_3$ in our samples is assumed to be presently calcite, but aragonitic $\delta^{44/40}$Ca and [Sr] values
347 could have been preserved if neomorphism occurred in low-porosity closed system conditions
348 during later diagenesis [*Husson et al.*, 2015].

349 The majority of the $\delta^{44/40}$Ca excursion in our sections likely represents the recovery from
350 the acidification event (when Ω is greater than background), not the acidification event itself
351 (when Ω is less than background) which is likely stratigraphically condensed given the sharpness
352 of the N1 excursion. Other sections are also potentially stratigraphically condensed or even
353 missing this interval given the globally observed decrease in carbonate sedimentation
354 [*Hautmann*, 2004] and that several localities do not capture the N1 excursion (see *Bachan et al.*
355 [2012] and *Greene et al.* [2012]. Our model predicts that the nadir of $\delta^{44/40}$Ca occurs when Ω is
356 at its maximum (Fig. 3). The maximum in Ω would be due to due to increased delivery of Ca^{2+}
357 via continental weathering as a result of higher pCO$_2$. Thus it is possible that aragonite would
358 have been more easily preserved shortly above the main extinction level, when Ω was greatest.

359 Of the scenarios listed above, local variation in f_a in T/J boundary sediments is the most
360 compatible with our data. Variable f_a has been proposed, in part, as the cause of a large (ca.
361 1.2‰), regional-scale negative $\delta^{44/40}$Ca excursion in the Ediacaran-age Wonoka Fm. of south
362 Australia [*Husson et al.*, 2015]. The Wonoka samples exhibit an inverse correlation between
363 $\delta^{44/40}$Ca and [Sr], similarly to the T/J boundary data. However, explaining the T/J boundary
364 $\delta^{44/40}$Ca excursion only by variation in f_a is incomplete. Local variation in mineralogy alone
365 cannot account for the associated mass extinction, the selective loss of heavily calcified marine
366 animals, the large, globally observed excursions in δ^{13}C, or the temporary increase in
367 atmospheric pCO$_2$. The carbon and calcium cycles are connected through the weathering and
368 burial of CaCO$_3$ and the dependency of weathering on pCO$_2$. Therefore, if large fluctuations in
369 δ^{13}C during the extinction event were caused by rapid injection of large volumes of CO$_2$ from
370 CAMP volcanism and the subsequent effects on carbonate saturation and organic carbon
371 production [*Hautmann et al.*, 2008; *Greene et al.*, 2012; *Honisch et al.*, 2012; *Martindale et al.*,
372 2012], it is likely they also affected seawater $\delta^{44/40}$Ca. Any mineralogical effects on $\delta^{44/40}$Ca
373 would therefore be *in addition* to primary seawater changes triggered by T/J events.

374   Given that the effects of acidification and changing mineralogy on $\delta^{44/40}$Ca may be
375 additive, we use our model results to estimate the relative impact of mineralogy on the $\delta^{44/40}$Ca
376 excursion. Assuming –0.14‰ of the observed $\delta^{44/40}$Ca excursion was from acidification (20% of
377 the full excursion), –0.58‰ would come from increasing f_a. Using an offset of 0.9‰ between
378 calcite and aragonite $\delta^{44/40}$Ca, this corresponds to a 64% increase in f_a during the negative
379 $\delta^{44/40}$Ca excursion.

380 **5 Conclusions**

381   We observe a ca. –0.8‰ excursion in $\delta^{44/40}$Ca preserved in the lowermost Jurassic
382 limestone sediments in the Lombardy Basin, northern Italy, immediately above the end-Triassic
383 extinction horizon. Numerical modeling of the coupled carbon and calcium cycles demonstrates
384 that the magnitude of the $\delta^{44/40}$Ca excursion is too large to have been caused solely by ocean
385 acidification resulting from emission of volcanic CO_2 during CAMP eruptions. Under a scenario
386 that best explains the δ^{13}C record and the associated evidence for increased pCO_2 and mass
387 extinction, roughly 80% of the T/J $\delta^{44/40}$Ca excursion at our locality is explained by locally
388 higher proportions of aragonite while the remainder reflects the consequences of ocean
389 acidification. Our study demonstrates that a coupled model of the carbon and calcium cycles can
390 be used to deconvolve the contributions of primary seawater isotopic changes and local effects
391 on sedimentary $\delta^{44/40}$Ca.

404 **References**

405 Bachan, A., and J. L. Payne (2015), Modelling the impact of pulsed CAMP volcanism on pCO2 and δ13C across the
406   Triassic–Jurassic transition, *Geol. Mag.*, *153*(June), 1–19, doi:10.1017/S0016756815000126.
407 Bachan, A., B. van de Schootbrugge, J. Fiebig, C. A. McRoberts, G. Ciarapica, and J. L. Payne (2012), Carbon cycle
408   dynamics following the end-Triassic mass extinction: Constraints from paired δ 13 C carb and δ 13 C org
409   records, *Geochemistry, Geophys. Geosystems*, *13*(9), n/a-n/a, doi:10.1029/2012GC004150.
410 Bachan, A., B. van de Schootbrugge, and J. L. Payne (2014), The end-Triassic negative δ13C excursion: A
411   lithologic test, *Palaeogeogr. Palaeoclimatol. Palaeoecol.*, *412*, 177–186, doi:10.1016/j.palaeo.2014.07.027.
412 Bartolini, A., J. Guex, J. E. Spangenberg, B. Schoene, D. G. Taylor, U. Schaltegger, and V. Atudorei (2012),
413   Disentangling the Hettangian carbon isotope record: Implications for the aftermath of the end-Triassic mass
414   extinction, *Geochemistry, Geophys. Geosystems*, *13*(1–11), doi:10.1029/2011GC003807.
415 Beerling, D. J., and R. A. Berner (2002), Biogeochemical constraints on the Triassic-Jurassic boundary carbon cycle
416   event, *Global Biogeochem. Cycles*, *16*(3), 10-1–10–13, doi:10.1029/2001GB001637.
417 Berner, R. A. (2004), *The Phanerozoic Carbon Cycle: CO2 and O2*, Oxford University Press, Oxford.
418 Blackburn, T. J., P. E. Olsen, S. A. Bowring, N. M. McLean, D. V Kent, J. Puffer, G. McHone, E. T. Rasbury, and

419   M. Et-Touhami (2013), Zircon U-Pb geochronology links the end-Triassic extinction with the Central Atlantic
420   Magmatic Province., *Science (80-.).*, *340*(6135), 941–5, doi:10.1126/science.1234204.
421   Blättler, C. L., G. M. Henderson, and H. C. Jenkyns (2012), Explaining the Phanerozoic Ca isotope history of
422   seawater, *Geology*, *40*(9), 843–846, doi:10.1130/G33191.1.
423   Brand, U., and J. Veizer (1980), Chemical diagenesis of a multicomponent carbonate system--1: Trace elements, *J.
424   Sediment. Res.*, *50*(4), 1219–1236.
425   Van Cappellen, P., and E. D. Ingall (1996), Redox stabilization of the atmosphere and oceans by phosphorus-limited
426   marine productivity, *Science*, *271*, 493–6.
427   DePaolo, D. J. (2004), Calcium isotopic variations produced by biological, kinetic, radiogenic and nucleosynthetic
428   processes, *Rev. Mineral. Geochemistry*, *55*, 255–288.
429   DePaolo, D. J. (2011), Surface kinetic model for isotopic and trace element fractionation during precipitation of
430   calcite from aqueous solutions, *Geochim. Cosmochim. Acta*, *75*(4), 1039–1056,
431   doi:10.1016/j.gca.2010.11.020.
432   Fantle, M. S. (2015), Calcium isotopic evidence for rapid recrystallization of bulk marine carbonates and
433   implications for geochemical proxies, *Geochim. Cosmochim. Acta*, *148*, 378–401,
434   doi:10.1016/j.gca.2014.10.005.
435   Farkaš, J., F. Böhm, K. Wallmann, J. Blenkinsop, A. Eisenhauer, R. Vangeldern, A. Munnecke, S. Voigt, and J.
436   Veizer (2007), Calcium isotope record of Phanerozoic oceans: Implications for chemical evolution of seawater
437   and its causative mechanisms, *Geochim. Cosmochim. Acta*, *71*(21), 5117–5134,
438   doi:10.1016/j.gca.2007.09.004.
439   Galli, M. T., F. Jadoul, S. M. Bernasconi, and H. Weissert (2005), Anomalies in global carbon cycling and
440   extinction at the Triassic/Jurassic boundary: evidence from a marine C-isotope record, *Palaeogeogr.
441   Palaeoclimatol. Palaeoecol.*, *216*(3–4), 203–214, doi:10.1016/j.palaeo.2004.11.009.
442   Galli, M. T., F. Jadoul, S. M. Bernasconi, S. Cirilli, and H. Weissert (2007), Stratigraphy and palaeoenvironmental
443   analysis of the Triassic–Jurassic transition in the western Southern Alps (Northern Italy), *Palaeogeogr.
444   Palaeoclimatol. Palaeoecol.*, *244*(1–4), 52–70, doi:10.1016/j.palaeo.2006.06.023.
445   Greene, S. E., R. C. Martindale, K. A. Ritterbush, D. J. Bottjer, F. A. Corsetti, and W. M. Berelson (2012),
446   Recognising ocean acidification in deep time: An evaluation of the evidence for acidification across the
447   Triassic-Jurassic boundary, *Earth-Science Rev.*, *113*(1–2), 72–93, doi:10.1016/j.earscirev.2012.03.009.
448   Griffith, E. M., M. S. Fantle, A. Eisenhauer, A. Paytan, and T. D. Bullen (2015), Effects of ocean acidification on
449   the marine calcium isotope record at the Paleocene-Eocene Thermal Maximum, *Earth Planet. Sci. Lett.*, *419*,
450   81–92, doi:10.1016/j.epsl.2015.03.010.
451   Gussone, N., F. Böhm, A. Eisenhauer, M. Dietzel, A. Heuser, B. Teichert, J. Reitner, G. Worheide, and W. Dullo
452   (2005), Calcium isotope fractionation in calcite and aragonite, *Geochim. Cosmochim. Acta*, *69*(18), 4485–
453   4494, doi:10.1016/j.gca.2005.06.003.
454   Hautmann, M. (2004), Effect of end-Triassic CO2 maximum on carbonate sedimentation and marine mass
455   extinction, *Facies*, *50*(2), 257–261, doi:10.1007/s10347-004-0020-y.
456   Hautmann, M. (2006), Shell mineralogical trends in epifaunal Mesozoic bivalves and their relationship to seawater
457   chemistry and atmospheric carbon dioxide concentration, *Facies*, *52*(3), 417–433, doi:10.1007/s10347-005-
458   0029-x.
459   Hautmann, M., M. J. Benton, and A. Tomašových (2008), Catastrophic ocean acidification at the Triassic-Jurassic
460   boundary, *Neues Jahrb. für Geol. und Paläontologie - Abhandlungen*, *249*(1), 119–127, doi:10.1127/0077-
461   7749/2008/0249-0119.
462   Hillebrandt, A. von et al. (2013), The Global Stratotype Sections and Point (GSSP) for the base of the Jurassic
463   System at Kuhjoch (Karwendel Mountains, Northern Calcareous Alps, Tyrol, Austria), *Episodes*, *36*(3), 162–
464   198.
465   Holmden, C., D. A. Papanastassiou, P. Blanchon, and S. Evans (2012), δ44/40Ca variability in shallow water
466   carbonates and the impact of submarine groundwater discharge on Ca-cycling in marine environments,
467   *Geochim. Cosmochim. Acta*, *83*, 179–194, doi:10.1016/j.gca.2011.12.031.
468   Honisch, B. et al. (2012), The geological record of ocean acidification, *Science (80-.).*, *335*(6072), 1058–1063,
469   doi:10.1126/science.1208277.
470   Horita, J., H. Zimmermann, and H. D. Holland (2002), Chemical evolution of seawater during the Phanerozoic:
471   Implications from the record of marine evaporites, *Geochim. Cosmochim. Acta*, *66*(21), 3373–3756.
472   Husson, J. M., J. A. Higgins, A. C. Maloof, and B. Schoene (2015), Ca and Mg isotope constraints on the origin of
473   Earth's deepest δ13C excursion, *Geochim. Cosmochim. Acta*, *160*, 243–266, doi:10.1016/j.gca.2015.03.012.
474   Kiessling, W., and C. Simpson (2011), On the potential for ocean acidification to be a general cause of ancient reef

475   crises, *Glob. Chang. Biol.*, *17*(1), 56–67, doi:10.1111/j.1365-2486.2010.02204.x.

476   Komar, N., and R. E. Zeebe (2011), Oceanic calcium changes from enhanced weathering during the Paleocene-
477   Eocene thermal maximum: No effect on calcium-based proxies, *Paleoceanography*, *26*(3), 1–13,
478   doi:10.1029/2010PA001979.

479   Komar, N., and R. E. Zeebe (2016), Calcium and calcium isotope changes during carbon cycle perturbations at the
480   end-Permian, *Paleoceanography*, (May 2015), 2015PA002834, doi:10.1002/2015PA002834.

481   Kump, L. R., and M. A. Arthur (1999), Interpreting carbon-isotope excursions: carbonates and organic matter,
482   *Chem. Geol.*, *161*, 181–198.

483   Lemarchand, D., G. J. Wasserburg, and D. A. Papanastassiou (2004), Rate-controlled calcium isotope fractionation
484   in synthetic calcite, *Geochim. Cosmochim. Acta*, *68*(22), 4665–4678, doi:10.1016/j.gca.2004.05.029.

485   Martindale, R. C., W. M. Berelson, F. A. Corsetti, D. J. Bottjer, and A. J. West (2012), Constraining carbonate
486   chemistry at a potential ocean acidification event (the Triassic–Jurassic boundary) using the presence of corals
487   and coral reefs in the fossil record, *Palaeogeogr. Palaeoclimatol. Palaeoecol.*, *350–352*, 114–123,
488   doi:10.1016/j.palaeo.2012.06.020.

489   McRoberts, C. A., L. Krystyn, and M. Hautmann (2012), Macrofaunal Response To the End-Triassic Mass
490   Extinction in the West-Tethyan Kossen Basin, Austria, *Palaios*, *27*(9), 607–616, doi:10.2110/palo.2012.p12-
491   043r.

492   Nielsen, L. C., J. L. Druhan, W. Yang, S. T. Brown, and D. J. DePaolo (2011), Calcium isotope as tracers of
493   biogeochemical processes, in *Handbook of Environmental Isotope Geochemistry*, edited by M. Baskaran, pp.
494   105–124, Springer-Verlag, Berlin Heidelberg.

495   Nielsen, L. C., D. J. Depaolo, and J. J. De Yoreo (2012), Self-consistent ion-by-ion growth model for kinetic
496   isotopic fractionation during calcite precipitation, *Geochim. Cosmochim. Acta*, *86*, 166–181,
497   doi:10.1016/j.gca.2012.02.009.

498   Paris, G., Y. Donnadieu, V. Beaumont, F. Fluteau, and Y. Goddéris (2016), Geochemical consequences of intense
499   pulse-like degassing during the onset of the Central Atlantic Magmatic Province, *Palaeogeogr.
500   Palaeoclimatol. Palaeoecol.*, *441*, 74–82, doi:10.1016/j.palaeo.2015.04.011.

501   Payne, J. L., A. V Turchyn, A. Paytan, D. J. DePaolo, D. J. Lehrmann, M. Yu, and J. Wei (2010a), Calcium isotope
502   constraints on the end-Permian mass extinction, *Proc. Natl. Acad. Sci.*, *107*(19), 8543–8548,
503   doi:10.1073/pnas.0914065107.

504   Payne, J. L., A. V. Turchyn, A. Paytan, D. J. DePaolo, D. J. Lehrmann, M. Yu, and J. Wei (2010b), Calcium isotope
505   constraints on the end-Permian mass extinction, *Proc. Natl. Acad. Sci.*, *107*(19), 8543–8548,
506   doi:10.1073/pnas.0914065107.

507   Raup, D. M., and J. J. Sepkoski (1982), Mass extinctions in the marine fossil record., *Science (80-.).*, *215*(4539),
508   1501–3, doi:10.1126/science.215.4539.1501.

509   Schaller, M. F., J. D. Wright, and D. V Kent (2011), Atmospheric PCO₂ perturbations associated with the Central
510   Atlantic Magmatic Province., *Science (80-.).*, *331*(6023), 1404–9, doi:10.1126/science.1199011.

511   Schaller, M. F., J. D. Wright, D. V. Kent, and P. E. Olsen (2012), Rapid emplacement of the Central Atlantic
512   Magmatic Province as a net sink for CO2, *Earth Planet. Sci. Lett.*, *323–324*, 27–39,
513   doi:10.1016/j.epsl.2011.12.028.

514   van de Schootbrugge, B., J. L. Payne, A. Tomasovych, J. Pross, J. Fiebig, M. Benbrahim, K. B. Föllmi, and T. M.
515   Quan (2008), Carbon cycle perturbation and stabilization in the wake of the Triassic-Jurassic boundary mass-
516   extinction event, *Geochemistry, Geophys. Geosystems*, *9*(4), n/a-n/a, doi:10.1029/2007GC001914.

517   Stanley, S. M. (2006), Influence of seawater chemistry on biomineralization throughout phanerozoic time:
518   Paleontological and experimental evidence, *Palaeogeogr. Palaeoclimatol. Palaeoecol.*, *232*(2–4), 214–236,
519   doi:10.1016/j.palaeo.2005.12.010.

520   Steinthorsdottir, M., A. J. Jeram, and J. C. McElwain (2011), Extremely elevated CO2 concentrations at the
521   Triassic/Jurassic boundary, *Palaeogeogr. Palaeoclimatol. Palaeoecol.*, *308*(3–4), 418–432,
522   doi:10.1016/j.palaeo.2011.05.050.

523   Tang, J., M. Dietzel, F. Böhm, S. J. Köhler, A. Eisenhauer, and M. Dietzel (2008), Sr2+/Ca2+ and 44Ca/40Ca
524   fractionation during inorganic calcite formation: II. Ca isotopes, *Geochim. Cosmochim. Acta*, *72*(15), 3733–
525   3745, doi:10.1016/j.gca.2008.05.033.

526   Veizer, J. A. N. (1983), Chemical diagenisis of carbonates: theory and application of trace element technique, *Stable
527   Isot. Sediment. Geol.*, Ch. 3.

528   Zeebe, R. E., and D. A. Wolf-Gladrow (2001), CO2 in seawater: equilibrium, kinetics, isotopes, *Elsevier Oceanogr.
529   Ser.*, *65*(65), 346, doi:10.1016/S0924-7963(02)00179-3.

530